Article | Open Access

Energy Materials

Min *et al. Energy Mater.* **2026**, *6*, 600014 **DOI:**10.20517/energymater.2025.189

Molybdenum and fluorine co-doping induces lattice oxygen activation in Ni-Fe spinel oxides for enhanced oxygen evolution

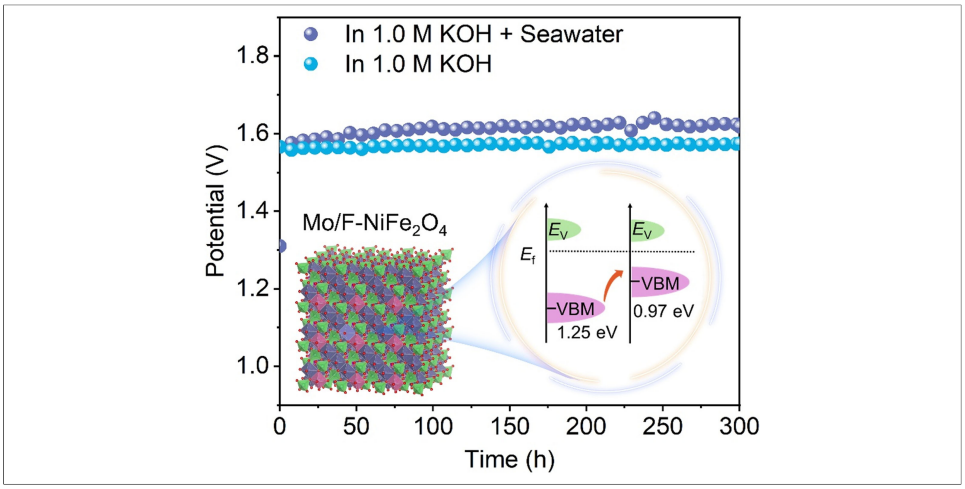
Xuehong Min[1,#], Luyao Wang[2,#], Hangning Liu[2,3], Xuyun Guo[4], Xinghang Liu[2], Yuhang Cheng[2], Valeria Nicolosi[4], Jie Wang[2,*]

Keywords:
$NiFe_2O_4$; cation-anion co-dopants; electrocatalysis; oxygen evolution reaction; lattice oxygen mechanism

Citation: Min, X.; Wang, L.; Liu, H.; Guo, X.; Liu, X.; Cheng, Y.; Nicolosi, V.; Wang, J. Molybdenum and fluorine co-doping induces lattice oxygen activation in Ni-Fe spinel oxides for enhanced oxygen evolution. *Energy Mater.* **2026**, *6*, 600014. https://dx.doi.org/10.20517/energymater.2025.189

Received: 7 Nov 2025 **First Decision:** 18 Dec 2025 **Revised:** 8 Jan 2025 **Accepted:** 21 Jan 2026 **Published:** 5 Feb 2026

Academic Editor: Ho Won Jang
Copy Editor: Fangling Lan
Production Editor: Fangling Lan



Abstract

The oxygen evolution reaction (OER) is a critical process in electrochemical water splitting, yet challenging in activation of lattice oxygen oxidation mechanism (LOM) for cost-effective transition metal oxides, in which strong metal-oxygen (M-O) bonds inherently inhibit lattice oxygen reactivity. Here, we design a molybdenum/fluorine (Mo/F) co-dopant in $NiFe_2O_4$ spinel to engineer the electronic structure via an LOM pathway. The incorporation of high-valence Mo and highly electronegative F collaboratively optimizes the electronic configuration of Ni/Fe sites, facilitating the formation of stable high-valent metal species and effectively weakening the M-O bonds. This synergy not only results in faster OER kinetics but also promotes oxygen vacancy formation, thereby enabling direct lattice oxygen involvement. Real-time ^{18}O-labeled differential electrochemical mass spectrometry coordinates with *in-situ* electrochemical impedance spectroscopy conclusively verify the activation of the LOM. The Mo/F-$NiFe_2O_4$ catalyst exhibits outstanding OER performance,

[1]Equine Science Research and Horse Doping Control Laboratory, Hubei Provincial Engineering Research Center of Racing Horse Detection and Application Transformation, Wuhan Business University, Wuhan 430056, Hubei, China.
[2]Qingdao Engineering Research Center of Agricultural Recycling Economy Materials, College of Chemistry and Pharmaceutical Sciences, Qingdao Agricultural University, Qingdao 266109, Shandong, China.
[3]School of Industrial and Information Engineering, Politecnico di Milano, Milano 20133, Italy.
[4]School of Chemistry, Centre for Research on Adaptive Nanostructures and Nanodevices (CRANN) and Advanced Materials Bio-Engineering Research Centre (AMBER), Trinity College Dublin, Dublin D02PN40, Ireland.
[#]Authors contributed equally.

[*]**Correspondence to:** Prof. Jie Wang, Qingdao Engineering Research Center of Agricultural Recycling Economy Materials, College of Chemistry and Pharmaceutical Sciences, Qingdao Agricultural University, Qingdao 266109, Shandong, China. E-mail: wangjie@qau.edu.cn

requiring low overpotentials of 247 and 311 mV to achieve current densities of 50 and 100 mA cm^{-2}, respectively. Remarkably, it demonstrates exceptional durability in seawater electrolytes, operating steadily for over 300 h at a high current density of 100 mA cm^{-2}. This work provides a general and effective doping strategy to activate the LOM in robust oxide catalysts, paving the way for efficient hydrogen production from both pure water and seawater resources.

INTRODUCTION

Green hydrogen, widely recognized as a clean and sustainable energy carrier, plays a pivotal role in the global transformation of the energy landscape[1-3]. The primary environmentally friendly and energy-effective strategy for large-scale production of hydrogen is water electrolysis driven by renewable energy sources[4-7]. However, the overall efficiency of this process is substantially constrained by the sluggish kinetics of the anodic oxygen evolution reaction (OER)[8-10] since it involves a complex four-electron transfer process. The sluggish kinetics necessitate high overpotentials in electrolyzers, leading to significant energy loss, not conducive to achieving global target of carbon peak and carbon neutrality[11-13]. This reaction predominantly follows the adsorbate evolution mechanism (AEM), in which oxygen-containing intermediates are sequentially adsorbed and desorbed at the same active site on the catalyst surface[14,15]. This pathway establishes intrinsic linear scaling relationships among the adsorption energies of these intermediates, thereby imposing a fundamental thermodynamic overpotential limit on the OER[16,17]. To overcome this limitation, the lattice oxygen oxidation mechanism (LOM) has emerged as a promising alternative[18,19]. By enabling direct participation of lattice oxygen from the catalyst in molecular oxygen formation, LOM bypasses the scaling relations inherent in AEM and offers a viable route to significantly enhance intrinsic OER activity[20-22]. Therefore, developing earth-abundant, cost-effective catalysts capable of activating lattice oxygen is crucial for scalable water splitting technologies.

In recent years, spinel oxides, particularly iron-based spinel (e.g., $FeCo_2O_4$, $NiFe_2O_4$, *etc.*), have emerged as highly promising electrocatalysts for the OER due to their low cost, earth abundance, and excellent electrical conductivity[23-25]. However, their intrinsic stable electronic structures and strong metal-oxygen bonds typically constrain the OER to the conventional AEM pathway, which limits catalytic efficiency[26,27]. This fundamental limitation highlights the critical need for precise electronic structure modulation to weaken metal-oxygen bonding and facilitate lattice oxygen activation, thereby promoting the transition from AEM to the more favorable LOM[28,29]. Heteroatom doping is widely recognized as an effective approach to modulate the electronic structure and enhance catalytic activity[30-33]. Among various dopants, high-valence molybdenum (Mo) and highly electronegative fluorine (F) have drawn significant attention due to their unique electronic characteristics[34-37]. Specifically, high-valence Mo can partially substitute metal cations in AB_2O_4 spinel lattice, effectively altering the electronic distribution and creating electron-rich or electron-deficient domains of catalyst interface, thereby optimizing the intrinsic activity for water oxidation[38,39]. Concurrently, the strong electron-withdrawing nature of F tends to distort the M-O bonding network, which facilitates lattice oxygen activation and promotes the LOM pathway[40,41]. Furthermore, the large-scale application and commercialization of alkaline water electrolysis require catalysts with not only high intrinsic activity but also long-term stability under practical operating conditions. However, under high current density operation, catalytic performance is often limited by structural degradation. Therefore, the development of spinel-based catalysts featuring precisely engineered structures, enhanced catalytic efficiency, and exceptional durability is crucial for sustainable water splitting at industrially relevant current densities - yet significant challenges remain.

In this study, we introduced molybdenum and fluorine dopants into the nickel-iron-based spinel

(Mo/F-$NiFe_2O_4$), aiming to enhance the oxygen evolution from a LOM pathway by cation-anion co-doping. Mo/F co-doping effectively elevates the valence band maximum of $NiFe_2O_4$, promoting activation of the LOM pathway during electrochemical OER. The Mo/F-$NiFe_2O_4$ catalyst shows excellent OER performance with low overpotentials of 247 and 311 mV to reach current densities of 50 and 100 mA cm^{-2}, respectively. It also exhibits remarkable stability in seawater electrolytes, maintaining stable operation for over 300 h at 100 mA cm^{-2}. Synchrotron radiation-based characterization and electron energy loss spectroscopy (EELS) confirmed the effective incorporation of Mo and F dopants, which promoted the formation of high-valence metal centers within the host lattice. X-ray photoelectron spectroscopy (XPS) and valence band measurements revealed that synergistic Mo/F co-doping shifted the maximum valence band (VBM) closer to the Fermi level. The upward VBM shift indicates a favorable electronic structure modification in the vicinity of the Fermi level, which is consistent with the observed changes in metal oxidation states from core-level spectroscopy and facilitates the activation of the LOM. Comprehensive electrochemical and physicochemical characterizations, supported by *in situ* electrochemical impedance spectroscopy (EIS) and ^{18}O-labeled differential electrochemical mass spectrometry (DEMS), consistently demonstrated that Mo/F co-doping effectively modulates the AB_2O_4 lattice to enhance lattice oxygen reactivity, accelerate reaction kinetics, and improve charge transfer efficiency. This work thus presents a highly efficient, fundamentally advanced, and scalable catalyst for the alkaline OER.

EXPERIMENTAL

Synthesis of Mo/F-$NiFe_2O_4$

First, nickel foam (NF) was pretreated and cut into pieces with size of 3 cm × 5 cm. 1.5 mmol of nickel nitrate hexahydrate, 3 mmol of ferric nitrate nonahydrate, 0.15 mmol of ammonium molybdate, 8 mmol of urea, 4 mmol of ammonium fluoride, and 2 mmol of glucose were dissolved in 35 mL of deionized water and magnetically stirred at room temperature for 0.5 h to ensure complete dissolution and homogeneity. The resulting solution was transferred to a 50 mL Teflon-lined stainless-steel autoclave containing the prepared NF substrate and heated at 120 °C for 12 h. After natural cooling to room temperature, the obtained precursor was thoroughly washed with deionized water and ethanol to remove residual ions, followed by vacuum drying at 60 °C. Finally, the dried precursor was annealed in a tube furnace under an argon atmosphere at a heating rate of 2 °C min^{-1} to 350 °C and held at that temperature for 2 h, yielding the Mo/F-$NiFe_2O_4$ catalyst.

Comparative catalysts including Mo-$NiFe_2O_4$, F-$NiFe_2O_4$, and $NiFe_2O_4$ were synthesized via the same approach without introducing ammonium fluoride, ammonium molybdate, or both, respectively.

RESULTS AND DISCUSSION

Scanning electron microscopy (SEM) was applied to study the microstructural evolution of various $NiFe_2O_4$-based catalysts. As illustrated in Figure 1A, pristine $NiFe_2O_4$ displays a flower-like morphology consisting of two-dimensional nanosheets with smooth surfaces. Upon Mo doping [Figure 1B], the overall flower-like architecture is retained; however, the nanosheets exhibit increased surface wrinkling and are decorated with small particles, resulting in enhanced surface roughness. In the case of F-doped $NiFe_2O_4$ [Figure 1C], the nanosheet-assembled flower-like structures demonstrate a significantly rougher surface, with well-distributed nanoparticles evident across the framework. In contrast, the Mo/F-$NiFe_2O_4$ [Figure 1D] preserves the flower-like morphology while displaying smoother, thinner and cleaner nanosheets, indicating that synergistic Mo and F co-doping effectively regulates the anisotropic growth of crystal planes. Scanning transmission electron microscopy (STEM) and high-resolution transmission electron microscopy (HRTEM) were further employed to investigate the detailed microstructure at higher magnifications. As shown in Figure 1E and Supplementary Figure 1A-D, all $NiFe_2O_4$-based catalysts exhibit nanosheet-like morphologies,

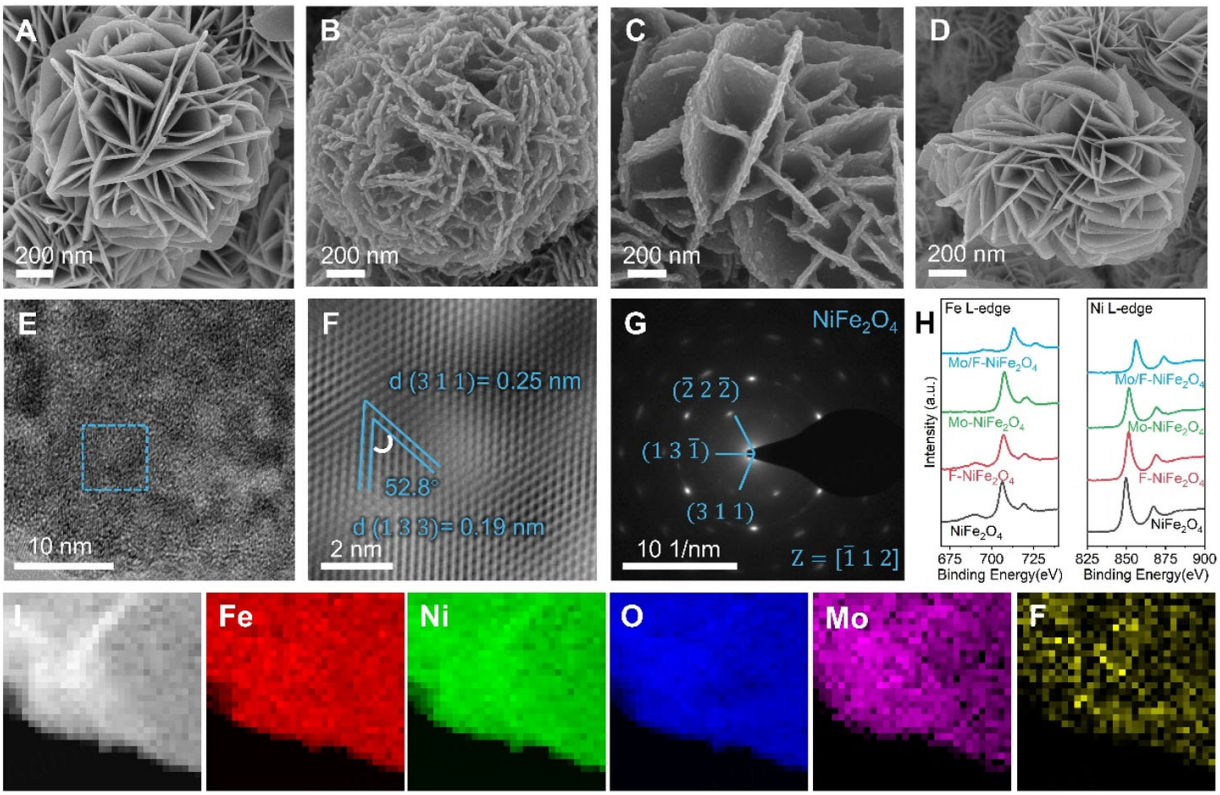


Figure 1. Morphology and structure characterizations of $NiFe_2O_4$-based catalysts. SEM images of (A) $NiFe_2O_4$, (B) Mo-$NiFe_2O_4$, (C)F-$NiFe_2O_4$ and (D) Mo/F-$NiFe_2O_4$; (E) TEM image, (F) iFFT-filtered HRTEM image, and (G) SAED pattern of Mo/F-$NiFe_2O_4$; (H) Ni L-edge and Fe L-edge EELS spectra of $NiFe_2O_4$, Mo-$NiFe_2O_4$, F-$NiFe_2O_4$ and Mo/F-$NiFe_2O_4$; (I) ADF-STEM and corresponding EELS maps of Mo/F-$NiFe_2O_4$.

consistent with the SEM observations. In Figure 1F, Mo/F-$NiFe_2O_4$ displays lattice fringes with spacings of 0.19 and 0.25 nm, which are assigned to the (1 3 3) and (3 1 1) planes of $NiFe_2O_4$, respectively, confirming its high crystallinity. This finding is further corroborated by the selected-area electron diffraction (SAED) pattern in Figure 1G, where distinct diffraction spots can be indexed to the ($\bar{2}$ 2 $\bar{2}$), (1 3 $\bar{1}$), and (3 1 1) planes of $NiFe_2O_4$. In comparison, Supplementary Figure 2A-C displays the HRTEM images of the other three catalysts. The $NiFe_2O_4$ exhibits lattice spacings of 0.24 and 0.25 nm, corresponding to the ($\bar{2}$ 2 $\bar{2}$) and (1 3 $\bar{1}$) lattice planes, respectively; the Mo-$NiFe_2O_4$ sample shows lattice spacings of 0.21 and 0.24 nm, corresponding to the (4 0 0) and (2 2 2) planes; while the F-$NiFe_2O_4$ sample also reveals lattice spacings of 0.21 and 0.25 nm, indexed to the (4 0 0) and (2 2 2) planes of $NiFe_2O_4$. Supplementary Figure 3A-C presents the corresponding SAED patterns, all of which are in good agreement with the HRTEM observations, further confirming the spinel structure of $NiFe_2O_4$. Energy-loss spectroscopy (EELS) spectra [Figure 1H] show that both the Ni-L and Fe-L edges, arising from 2p → 3d electronic transitions, shift to higher energy losses upon Mo/F co-doping relative to the pristine spinel. This shift indicates an increase in the average oxidation states of Ni and Fe, as well as enhanced metal–oxygen covalency, driven by electron redistribution among Ni, Fe, Mo, and F species. Figure 1I presents the annular dark field (ADF)-STEM image and corresponding elemental mapping images of the Mo/F-$NiFe_2O_4$ catalyst, revealing a homogeneous distribution of Mo and F throughout the structure. Consistently, Supplementary Figure 4 further confirms the uniform incorporation of Mo and F dopants.

The phase structure and chemical composition of the $NiFe_2O_4$-based catalysts was further investigated at bulk aspects. The X-ray diffraction (XRD) pattern shown in Supplementary Figure 5A displays diffraction

peaks at 30.3°, 35.6°, and 63.1°, assigned to the (220), (311), and (440) crystal planes of $NiFe_2O_4$ spinel (PDF No. 10-0325), respectively. In addition, weak diffraction peaks observed at 44.2°, 51.2°, and 76.4° correspond to the (111), (200), and (220) planes of metallic Ni (PDF No. 04-0850), which are attributed to the underlying NF substrate. Meanwhile, as shown in Figure 2A, Supplementary Figure 5, and Supplementary Table 1, the refined lattice parameter increased from 8.32163 Å ($NiFe_2O_4$) to 8.34101 Å for the Mo/F-$NiFe_2O_4$. This lattice expansion provides direct structural evidence for the successful incorporation of Mo and F into the spinel framework. To further verify the phase composition and surface chemical states, XPS measurements were performed. As shown in Supplementary Figure 6, the survey XPS spectrum confirms the presence of Ni, Fe, O, Mo, and F in the heteroatom-doped catalysts. As shown in Supplementary Table 2, relative to the undoped $NiFe_2O_4$ (23.29%), F-doping significantly increases the surface oxygen content (63.12%), while Mo-doping alone results in a considerably smaller change (29.45%). Importantly, the Mo/F co-doped catalyst attains an optimal, intermediate oxygen content (33.54%). This state of balance is of crucial importance as it adequately activates the lattice oxygen mechanism to boost activity while preventing excessive lattice oxygen that might undermine structural stability during operation[42]. High-resolution O 1s spectra of different catalysts are presented in Figure 2B, revealing three distinct peaks at 529.8, 531.2, and 532.3 eV, assigned to lattice oxygen (M-O), oxygen vacancies (O_V), and adsorbed water species, respectively[43]. The specific atomic content of different oxygen species can be seen in Supplementary Table 3. Notably, the binding energy of the M-O peak gradually decreases with Mo and F doping. Specifically, the Mo/F-$NiFe_2O_4$ exhibits a 0.50 eV negative shift compared to pristine $NiFe_2O_4$, whereas the single-doped Mo-$NiFe_2O_4$ and F-$NiFe_2O_4$ samples display smaller shifts of 0.30 and 0.10 eV, respectively. As shown in Supplementary Figure 7, the Ni 2p spectrum exhibits characteristic peaks at 852.8, 855.2, 856.4, 861.1 and 863 eV, which are attributed to Ni^0, Ni^{2+}, Ni^{3+}, and the satellite peak, respectively[44-46]. Likewise, Supplementary Figure 8 presents the Fe 2p spectrum with distinct peaks at 710.8, 713.2, and 717.3 eV, assigned to Fe^{2+}, Fe^{3+}, and their corresponding satellite feature[47-49], respectively. To confirm the successful incorporation of Mo and F dopants, Mo 3d and F 1s XPS spectra were acquired. As shown in Supplementary Figure 9, the Mo 3d spectra of both Mo-$NiFe_2O_4$ and Mo/F-$NiFe_2O_4$ exhibit well-resolved doublet peaks at 232.1 and 235.2 eV, which are assigned to Mo $3d_{5/2}$ and Mo $3d_{3/2}$, respectively, confirming the presence of Mo^{6+} species[50,51]. Similarly, the high-resolution F 1s spectra [Supplementary Figure 10] display a sharp peak at 684.0 eV, which is characteristic of M-F, thereby verifying the successful substitution of F into the crystal structure[52]. To investigate the impact of doping on the electronic band structure, XPS valence band spectra were analyzed [Figure 2C]. The energy difference between the VBM and the Fermi level is 1.25 eV for pristine $NiFe_2O_4$. In contrast, the VBM of Mo/F-$NiFe_2O_4$ shifts upward to 0.97 eV, whereas Mo-$NiFe_2O_4$ and F-$NiFe_2O_4$ exhibit smaller shifts of 1.18 and 1.21 eV, respectively. This upward shift in the VBM of the Mo/F co-doped sample suggests a reduced difficulty in excitation of valence electrons to the Fermi level, promoting more efficient charge transfer and accelerating reaction kinetics. As a result, Mo/F-$NiFe_2O_4$ demonstrates reduced charge-transfer resistance and improved intrinsic OER activity. X-ray absorption spectroscopy (XAS) based on synchrotron radiation was employed to study the local coordination environment and valence state variations of the catalysts. As shown in Figure 2D, the Mo/F-$NiFe_2O_4$ exhibits a higher Ni K-edge energy compared to both $NiFe_2O_4$ and Ni foil, indicating that the dual synergistic modulation by Mo and F promotes the formation of higher-valence Ni species in $NiFe_2O_4$. These high-valence Ni species are conducive to enhancing the intrinsic OER activity and facilitating the activation of the LOM[53,54]. The k^3-weighted Fourier-transformed extended X-ray absorption fine structure (FT-EXAFS) spectra of Mo/F-$NiFe_2O_4$ and pristine $NiFe_2O_4$ [Figure 2E] reveal not only the characteristic Ni-O and Ni-Ni coordination shells but also additional Ni-Mo and Ni-F scattering paths, further confirming the successful incorporation of Mo and F into the lattice structure[54]. This structural modification suggests that under dual modulation of Mo and F, the Ni-O bond energy is reduced, facilitating bond cleavage. These observations are supported by wavelet transform (WT) analyses in Figure 2F and Supplementary Figure 11. Similarly, as shown in the Fe K-edge of Figure 2G, Mo/F-$NiFe_2O_4$ exhibits a higher oxidation state at the Fe K-edge compared to both $NiFe_2O_4$ and Fe foil, further indicating that the synergistic

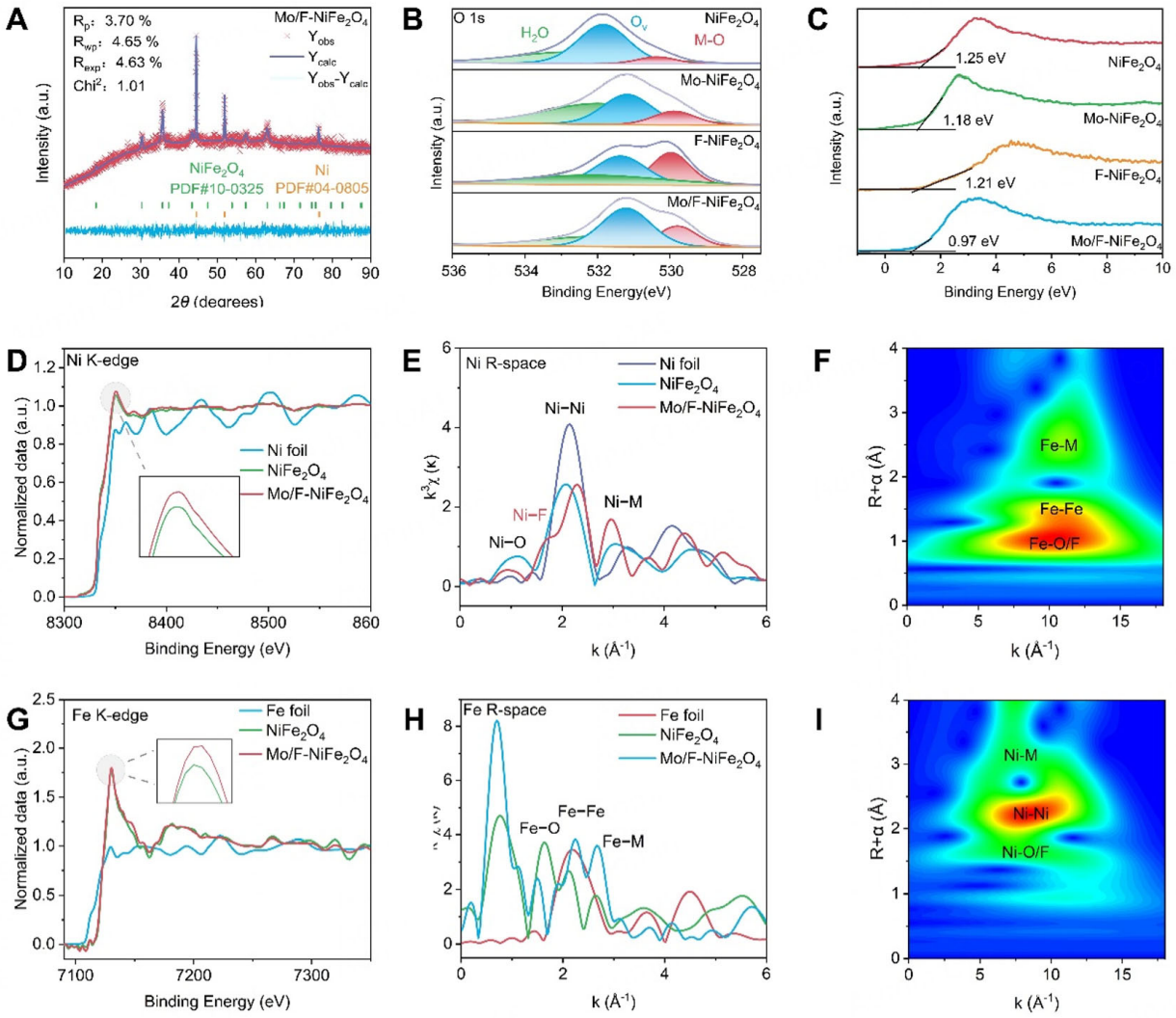


Figure 2. Physical properties of Mo/F-$NiFe_2O_4$. (A) XRD Rietveld refinement patterns; (B) High-resolution O 1s XPS spectrum; (C) XPS valence band spectrum; (D) XANES spectra of Ni K-edge; (E) Ni R-space EXAFS spectra; (F) WT analysis of Mo/F-$NiFe_2O_4$; (G) XANES spectra of Fe K-edge; (H) Fe R-space EXAFS spectra; (I) WT analysis of Mo/F-$NiFe_2O_4$.

incorporation of Mo and F promotes the formation of higher-valence Fe species in $NiFe_2O_4$, which is conducive to activating the LOM[55]. The FT-EXAFS spectra [Figure 2H] of Mo/F-$NiFe_2O_4$ and pristine $NiFe_2O_4$ reveal additional Fe-M and Fe-F coordination shells beyond the typical Fe-O and Fe-Fe bonds, providing direct evidence for the successful doping of Mo and F into the structure. Furthermore, the dual modulation by Mo and F weakens the Fe-O bond strength, thereby facilitating its cleavage during catalytic processes[55]. These observations are consistent with the WT analyses presented in Figure 2I and Supplementary Figure 12.

The electrocatalytic OER performance of the synthesized $NiFe_2O_4$-based catalysts and commercial RuO_2 was evaluated in 1.0 M KOH solution. As shown from the polarization curves in Figure 3A and Supplementary Figure 13, Mo/F-$NiFe_2O_4$ exhibits superior OER activity compared with all other catalysts synthesized under the same conditions and RuO_2. Specifically, Mo/F-$NiFe_2O_4$ delivers current densities of 50 and 100 mA cm^{-2} at overpotentials of 245 and 311 mV, which are significantly lower than those of Mo-$NiFe_2O_4$, F-$NiFe_2O_4$, $NiFe_2O_4$, and commercial RuO_2 [Figure 3B]. The Tafel slope was further employed to assess the electron transfer kinetics during the OER, in which Mo/F-$NiFe_2O_4$ exhibits the lowest Tafel

slope (49.68 mV dec^{-1}) among the tested catalysts, compared to Mo-$NiFe_2O_4$ (53.78 mV dec^{-1}), F-$NiFe_2O_4$ (67.24 mV dec^{-1}), and $NiFe_2O_4$ (71.15 mV dec^{-1}), indicating more efficient OER kinetics under alkaline conditions [Figure 3C]. The properties at the catalytic interface were studied via evaluation of the electrochemical active surface area (ECSA) and normalized kinetic current (j_K^{norm}) since the ECSA is linearly proportional to the double-layer capacitance (C_{dl}) at non-Faradic potential range. Cyclic voltammetry (CV) curves with a non-Faradic potential range of 0.5 V-0.6 V at varying scan rates [Supplementary Figure 14]. As illustrated in Figure 3D, Mo/F-$NiFe_2O_4$ exhibits a C_{dl} value of 2.11 mF cm^{-2}, which is higher than that of $NiFe_2O_4$ (1.46 mF cm^{-2}) and NF (1.14 mF cm^{-2}), but much lower than those of Mo-$NiFe_2O_4$ (18.20 mF cm^{-2}) and F-$NiFe_2O_4$ (5.45 mF cm^{-2}). This indicates that Mo/F co-doping does not confer a substantial advantage in terms of ECSA. The higher C_{dl} values observed for Mo-$NiFe_2O_4$ and F-$NiFe_2O_4$ can be attributed to their comparatively rougher nanoparticle morphologies, as revealed by the SEM images in Figure 1. However, when the kinetic current density (j) is normalized by the C_{dl} value at a fixed potential of 1.48 V, Mo/F-$NiFe_2O_4$ displays the highest j_K^{norm} value (24.31 mA mF^{-1}), outperforming Mo-$NiFe_2O_4$ (1.75 mA mF^{-1}), F-$NiFe_2O_4$ (5.12 mA mF^{-1}), $NiFe_2O_4$ (15.54 mA mF^{-1}) and NF (0.12 mA mF^{-1}). This result clearly demonstrates that the superior intrinsic OER activity of Mo/F-$NiFe_2O_4$ stems from its optimally engineered electronic structure with appropriate ECSA. To elucidate the kinetic differences, EIS was employed to evaluate the charge transfer kinetics during the OER [Figure 3E]. As shown in Supplementary Figure 15, the equivalent circuit model was used to deconvolute the two distinct electrochemical processes occurring at the electrode/electrolyte interface. Among all synthesized catalysts, Mo/F-$NiFe_2O_4$ exhibits the lowest charge transfer resistance (R_{ct}) of 3.1 Ω, which is lower than those of Mo-$NiFe_2O_4$ (3.6 Ω), F-$NiFe_2O_4$ (3.7 Ω), and pristine $NiFe_2O_4$ (3.8 Ω), indicating superior charge transfer efficiency and enhanced OER kinetics. In addition to activity, stability represents another critical parameter for assessing OER performance. The long-term durability of Mo/F-$NiFe_2O_4$ was evaluated through a chronopotentiometric test (V-t curve) at a high current density of 100 mA cm^{-2} [Figure 3F]. The catalyst exhibited stable OER performance over 130 h of continuous operation, underscoring its exceptional durability. Notably, the OER performance of Mo/F-$NiFe_2O_4$ outperforms that of most recently reported alkaline OER catalysts in the literature [Figure 3G and Supplementary Table 4].

To verify whether Mo/F-$NiFe_2O_4$ activates the LOM during the OER, DEMS measurements were performed in real-time on both Mo/F-$NiFe_2O_4$ and pristine $NiFe_2O_4$ [Figure 4A and B]. Using 99.99% $H_2{}^{18}O$ as the solvent in a 1 M KOH electrolyte, a distinct signal was detected at m/z = 34 ($^{16}O^{18}O$) for Mo/F-$NiFe_2O_4$ during OER, whereas the signal at m/z = 36 ($^{18}O_2$) was negligible. In contrast, pristine $NiFe_2O_4$ showed no detectable signal at m/z = 34 but exhibited a prominent peak at m/z = 36 ($^{18}O_2$), indicating exclusive involvement of labeled oxygen from the electrolyte. These results clearly demonstrate that the synergistic modulation of Mo and F promotes the activation of the LOM in $NiFe_2O_4$ spinel, thereby significantly enhancing its intrinsic catalytic activity. To observe the structural evolution after the stability test, Raman spectroscopy was conducted before and after OER stability test. As clearly shown in Figure 4C, the pre-reaction sample displayed distinct characteristic peaks at approximately 621 and 1,154 cm^{-1}, which corresponded to $NiFe_2O_4$. In sharp contrast, the post-reaction catalyst presented a double peak around 551 and 678 cm^{-1}. Previous research findings indicate that these peaks correspond to the characteristic peaks of NiFeOOH, which strongly suggests a certain degree of surface reconstruction at the interface during the reaction[26]. To further confirm the occurrence of surface reconstruction, XPS characterization was carried out on Mo/F-$NiFe_2O_4$ before and after the OER stability test. As depicted in Figure 4D and E, the relative content of oxygen vacancy species in the post-reconstruction sample increased from 50.07% to 61.21%, whereas the content of lattice oxygen species decreased from 26.01% to 6.77%. This firmly confirms the occurrence of surface reconstruction and further validates the LOM pathway. Furthermore, to gain deeper insight into the kinetic behavior of the catalytic process, *in situ* EIS was conducted [Figure 4F-I]. Analysis of the relaxation time and impedance magnitude reveals that Mo/F-$NiFe_2O_4$ exhibits the lowest R_{ct} and the

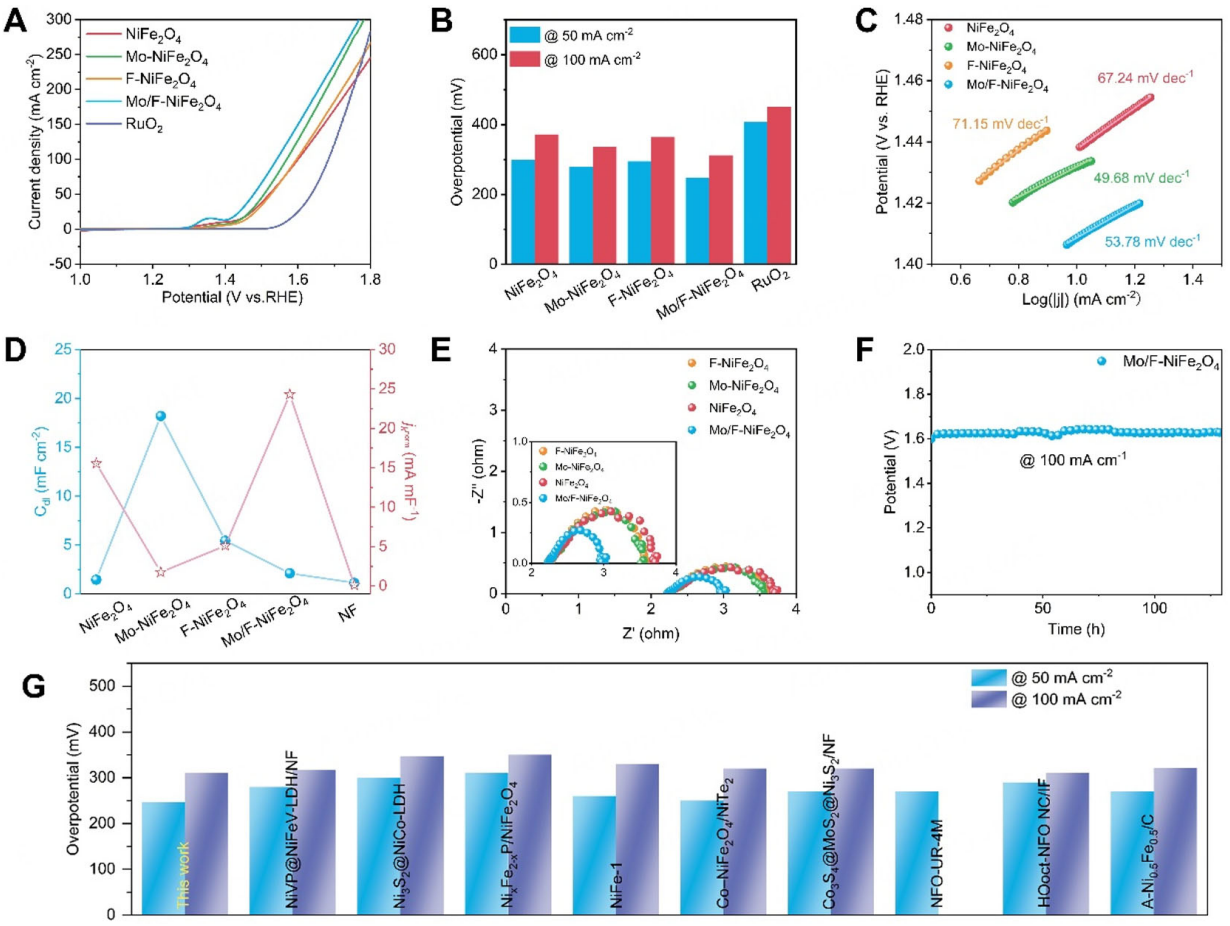


Figure 3. OER catalytic performance of Mo/F-$NiFe_2O_4$. (A) Polarization curves; (B) Histogram of overpotentials at current densities of 50.0 and 100.0 mA cm^{-2}; (C) Tafel plots; (D) Dot-line plots of C_{dl} (blue), and j_K^{norm} (red) at potential of 1.48 V; (E) Nyquist plots; (F) Time-dependent potential curves at a constant current density of 100 mA cm^{-2} for over 130 h; (G) A comprehensive comparison of with recently reported other catalysts.

fastest reaction kinetics among all catalysts, outperforming Mo-NFe_2O_4, F-$NiFe_2O_4$ and pristine $NiFe_2O_4$. These findings confirm that the superior intrinsic activity and accelerated reaction kinetics of Mo/F-iFe_2O_4 are directly attributed to the activation of the LOM.

A two-electrode configuration was employed to evaluate the potential of the electrocatalyst for overall water splitting, in which the synthesized catalyst served as anode and commercial Pt/C as cathode. In this configuration, water oxidation occurs at the anode, where OH^- ions are converted into O_2, while hydrogen evolution takes place at the cathode, producing H_2. Electrochemical measurements were performed in both 1.0 M KOH and alkaline seawater electrolytes. As shown in Figure 5A, under 1.0 M KOH conditions, the polarization curves of the optimized Mo/F-$NiFe_2O_4$ and commercial RuO_2 were performed for comparison. Specifically, the overall water-splitting voltages for Mo/F-$NiFe_2O_4$ were 1.54 and 1.59 V at current densities of 50 and 100 mA cm^{-2}, respectively, lower than those of commercial RuO_2 (1.60 and 1.66 V). Meanwhile, as illustrated in Figure 5B, in alkaline seawater, Mo/F-$NiFe_2O_4$ achieved a current density of 100 mA cm^{-2} at only 1.65 V, highlighting its superior intrinsic catalytic activity. Considering working stability is another key criterion for assessing catalytic performance, the stability test at both alkaline and alkaline seawater electrolytes was performed. As shown in Figure 5C, the chronoamperometric test in 1.0 M KOH revealed

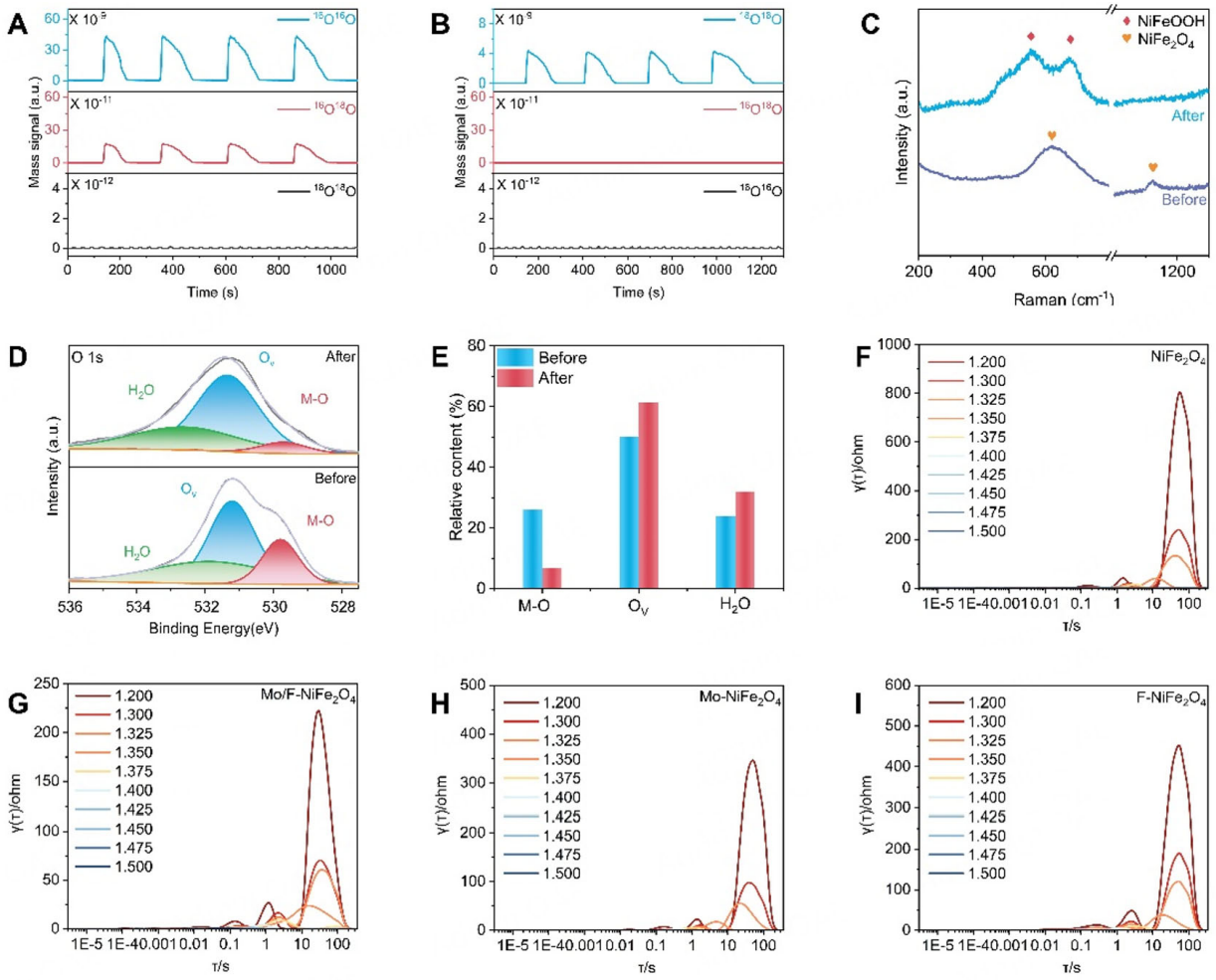


Figure 4. Verification of the LOM pathway and interface changes of Mo/F-$NiFe_2O_4$. DEMS of (A) Mo/F-$NiFe_2O_4$ and (B) $NiFe_2O_4$; (C) Raman spectra ; (D) High-resolution XPS O 1s spectra; (E) Relative content of the different oxygen species of the Mo/F-$NiFe_2O_4$ before and after stability test; *In-situ* impedance testing diagram with corresponding relaxation time distribution diagram of (F) $NiFe_2O_4$, (G) Mo-$NiFe_2O_4$, (H) F-$NiFe_2O_4$ and (I) Mo/F-$NiFe_2O_4$.

that Mo/F Mo/F-$NiFe_2O_4$ exhibited negligible voltage fluctuations over 300 h of continuous operation. Similarly, Figure 5D demonstrates that under alkaline seawater conditions, Mo/F-$NiFe_2O_4$ maintained exceptional stability for more than 300 h at a high current density of 100 mA cm^{-2}, demonstrating excellent adaptability to complex environments and practical potential for industrial production. Additionally, to further evaluate the catalyst's resistance to chlorine-related side reactions and OER-related Faraday efficiency (FE), iodination colorimetric reaction was performed. As shown in Supplementary Figure 16, Mo/F-$NiFe_2O_4$ exhibited negligible color change after exposure to the post-reaction electrolyte solution. In contrast, RuO_2 turned pale yellow after the stability test. This indicates that Mo/F-$NiFe_2O_4$ possesses excellent performance in suppressing competing chlorine (ClO^-) side reactions. The oxygen FE of Mo/F-$NiFe_2O_4$ was calculated using the displacement gas collection method [Supplementary Equation 2]. The pre-reaction FE [Supplementary Figure 17] was 96.6%, while the post-reaction efficiency was 93.1%, showing no significant decrease and demonstrating the outstanding OER stability of Mo/F-$NiFe_2O_4$.

CONCLUSIONS

In summary, Mo/F-$NiFe_2O_4$ was successfully constructed for the OER in alkaline media. Mo/F co-doping modulated the electronic structure, increased Ni/Fe oxidation states, and shifted the VBM upward, inducing

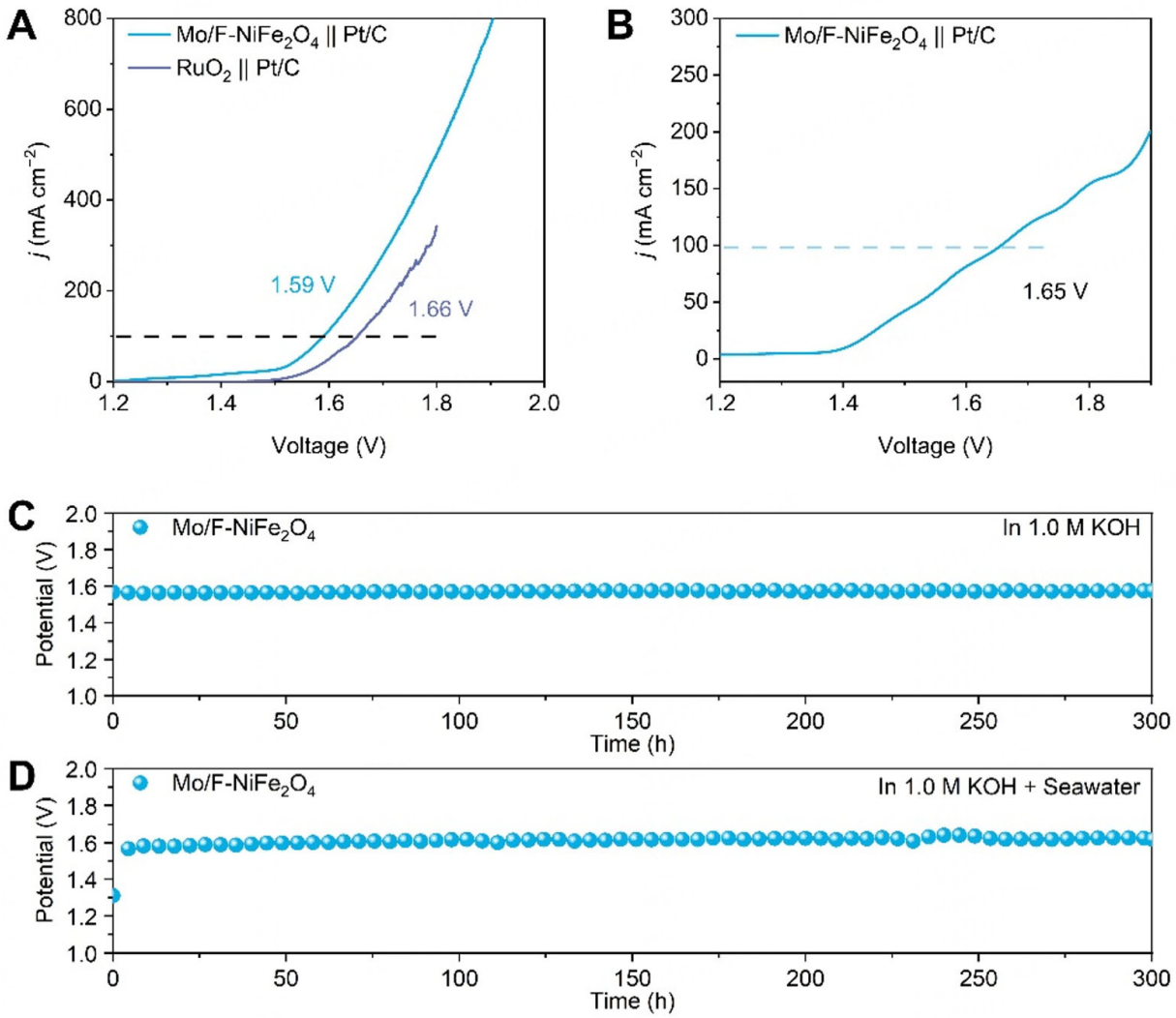


Figure 5. Overall water splitting performance of Mo/F-$NiFe_2O_4$. (A) Polarization curves in 1.0 M KOH; (B) Polarization curves in 1.0 M KOH + Seawater; (C) Illustration of chronopotentiometric stability test in 1.0 M KOH. (D) Illustration of chronopotentiometric stability test in 1.0 M KOH + Seawater.

electron redistribution and weakening metal-oxygen bonds, thereby facilitating M-O bond formation and cleavage during catalysis. Furthermore, Mo/F-$NiFe_2O_4$ catalyst effectively activated LOM, leading to accelerated reaction kinetics and enhanced intrinsic activity. Owing to these synergistic effects, the optimized Mo/F-$NiFe_2O_4$ catalyst delivered a low overpotential of 247 mV at 50 mA cm^{-2}, and outstanding long-term stability over 130 h at 100 mA cm^{-2}, surpassing both pristine $NiFe_2O_4$ and single-doped counterparts. Practical water-splitting in both alkaline and alkaline seawater demonstrated improved activity and stability. This work shows case insights into how dual anion-cation co-dopants in regulating lattice oxygen participation in the OER, offering valuable guidance for practical water electrolysis applications.

DECLARATIONS

Acknowledgments

The authors thank the Analytical and Testing Center of Qingdao Agricultural University for allowing the use of its facilities. We also thank Beijing SciStar Technology Co., Ltd. for XAFS measurements and analysis. Furthermore, Nicolosi, V. and Guo, X. acknowledge the Advanced Microscopy Laboratory (AML) at CRANN for access to their facilities.

Authors' contributions

Made substantial contributions to design of the study and performed writing: Min, X.; Wang, L.; Wang, J.

Assist in processing and analyzing data: Min, X.; Wang, L.; Liu, H.; Liu, X.; Guo, X.; Nicolosi, V.
Collected literature: Wang, L.; Liu, H.; Guo, X.; Cheng, Y.
Assist in collecting literature and researching the background: Min, X.; Wang, L.; Liu, H.
Made substantial contributions to conception of the study and provided financial support: Min, X.; Wang, J.
Revised the logic and grammar of the article: Nicolosi, V.; Wang, J.

Availability of data and materials

The relevant data and materials for the results of this study can be obtained from the first author or corresponding author upon reasonable request.

Financial support and sponsorship

This work was financially supported by the Natural Science Foundation of Shandong Province (Nos. ZR2022QB028 and ZR2025MS141), the National Natural Science Foundation of China (No. 22202114), the Natural Science Foundation of Hubei Province of China (No. 2024AFB870), the PhD Research Fund Project of Wuhan Business University (No. 2023KB009), and the project Research and Development of Testing Standards for Prohibited Substances in Sports Horses (No. 2024TD021). V.N. and X.G. acknowledge support from the Research Ireland-funded AMBER Research Centre and the SFI Frontiers for the Future program (Grant Nos. 12/RC/2278_P2 and 20/FFP-A/8950, respectively). V.N. and X.G. also acknowledge the Advanced Microscopy Laboratory (AML) at CRANN for access to facilities and thank Clive Downing for assistance with microscope optimization.

Conflicts of interest

All authors declared that there are no conflicts of interest.

Ethical approval and consent to participate

Not applicable.

Consent for publication

Not applicable.

Copyright

© The Author(s) 2026.

Supplementary Materials

Supplementary Materials

REFERENCES

1. Yang, Y.; Li, P.; Zheng, X.; et al. Anion-exchange membrane water electrolyzers and fuel cells. *Chem. Soc. Rev.* **2022**, *51*, 9620-93. DOI PubMed
2. Xu, H.; Yuan, J.; He, G.; Chen, H. Current and future trends for spinel-type electrocatalysts in electrocatalytic oxygen evolution reaction. *Coord. Chem. Rev.* **2023**, *475*, 214869. DOI
3. Yue, K.; Lu, R.; Gao, M.; et al. Polyoxometalated metal-organic framework superstructure for stable water oxidation. *Science* **2025**, *388*, 430-6. DOI PubMed
4. Liu, H.; Liu, X.; Sun, A.; et al. Enhancing oxygen evolution electrocatalysis in heazlewoodite: unveiling the critical role of entropy levels and surface reconstruction. *Adv. Mater.* **2025**, *37*, e2501186. DOI PubMed PMC
5. Lu, M.; Zheng, Y.; Hu, Y.; et al. Artificially steering electrocatalytic oxygen evolution reaction mechanism by regulating oxygen defect contents in perovskites. *Sci. Adv.* **2022**, *8*, eabq3563. DOI PubMed PMC
6. Li, P.; Mao, Y.; Shin, H.; et al. Tandem amine scrubbing and CO_2 electrolysis via direct piperazine carbamate reduction. *Nat. Energy.* **2025**, *10*, 1262-73. DOI
7. Sun, Y.; Sun, Z.; Zhang, W.; et al. Fabricating freestanding electrocatalyst with bismuth-iron dual active sites for efficient ammonia synthesis in neutral media. *EcoEnergy* **2023**, *1*, 186-96. DOI
8. Lu, Z.; Chen, G.; Siahrostami, S.; et al. High-efficiency oxygen reduction to hydrogen peroxide catalysed by oxidized carbon materials. *Nat. Catal.* **2018**, *1*, 156-62. DOI

9. Luo, X.; Zhao, H.; Tan, X.; et al. Fe-S dually modulated adsorbate evolution and lattice oxygen compatible mechanism for water oxidation. *Nat. Commun.* **2024**, *15*, 8293. DOI PubMed PMC
10. Malinovic, M.; Paciok, P.; Koh, E. S.; et al. Size-controlled synthesis of IrO_2 nanoparticles at high temperatures for the oxygen evolution reaction. *Adv. Energy. Mater.* **2023**, *13*, 2301450. DOI
11. Mei, Y.; Chen, J.; Wang, Q.; et al. MoZn-based high entropy alloy catalysts enabled dual activation and stabilization in alkaline oxygen evolution. *Sci. Adv.* **2024**, *10*, eadq6758. DOI PubMed PMC
12. Sun, W.; Wang, Y.; Liu, S.; Lei, F.; Xie, J.; Tang, B. High-entropy amorphous oxycyanide as an efficient pre-catalyst for the oxygen evolution reaction. *Chem. Commun.* **2022**, *58*, 11981-4. DOI PubMed
13. Xia, W.; Ming, C.; Shuang, L.; et al. Sea urchin-like La-doped MnO_2 for electrocatalytic oxidation degradation of sulfonamide in water. *Energy. Mater.* **2025**, *5*, 500150. DOI
14. Zhang, G.; Pei, J.; Wang, Y.; et al. Selective activation of lattice oxygen site through coordination engineering to boost the activity and stability of oxygen evolution reaction. *Angew. Chem. Int. Ed.* **2024**, *63*, e202407509. DOI PubMed
15. Zheng, W.; Liang, G.; Liu, Q.; et al. The promise of high-entropy materials for high-performance rechargeable Li-ion and Na-ion batteries. *Joule* **2023**, *7*, 2732-48. DOI
16. Olowoyo, J. O.; Kriek, R. J. Recent progress on bimetallic-based spinels as electrocatalysts for the oxygen evolution reaction. *Small* **2022**, *18*, e2203125. DOI PubMed
17. Liu, S.; Shi, Y.; Wang, D.; et al. Multiple synergies on cobalt-based spinel oxide nanowires for electrocatalytic oxygen evolution. *J. Colloid. Interface. Sci.* **2024**, *655*, 685-92. DOI PubMed
18. Huang, Z. F.; Xi, S.; Song, J.; et al. Tuning of lattice oxygen reactivity and scaling relation to construct better oxygen evolution electrocatalyst. *Nat. Commun.* **2021**, *12*, 3992. DOI PubMed PMC
19. Chang, C. W.; Ting, Y. C.; Yen, F. Y.; Li, G. R.; Lin, K. H.; Lu, S. Y. High performance anion exchange membrane water electrolysis driven by atomic scale synergy of non-precious high entropy catalysts. *Energy. Mater.* **2025**, *5*, 500117. DOI
20. Seenivasan, S.; Kim, M.; Han, J. W.; Kim, D. Minimal doping approach to activate lattice oxygen participation in K_2WO_4 electrocatalysts for oxygen evolution reaction. *Appl. Catal. B. Environ. Energy.* **2024**, *358*, 124423. DOI
21. Wang, X.; Hu, J.; Lu, T.; et al. Importing atomic rare-earth sites to activate lattice oxygen of spinel oxides for electrocatalytic oxygen evolution. *Angew. Chem. Int. Ed.* **2025**, *64*, e202415306. DOI PubMed PMC
22. Hu, Z.; Wu, H.; Yong, X.; et al. Advances in dual-site mechanisms for designing high-performance oxygen evolution electrocatalysts. *eScience* **2025**, *5*, 100403. DOI
23. Einert, M.; Sezen, H.; Wu, Q.; et al. $NiFe_2O_4$ spinel thin film electrocatalysts: ordered mesoporous networks for driving the oxygen evolution reaction. *ACS. Appl. Nano. Mater.* **2025**, *8*, 14218-29. DOI
24. Feng, Z.; Wang, P.; Cheng, Y.; et al. Recent progress on $NiFe_2O_4$ spinels as electrocatalysts for the oxygen evolution reaction. *J. Electroanal. Chem.* **2023**, *946*, 117703. DOI
25. Zhong, H.; Gao, G.; Wang, X.; et al. Ion irradiation inducing oxygen vacancy-rich NiO/$NiFe_2O_4$ heterostructure for enhanced electrocatalytic water splitting. *Small* **2021**, *17*, e2103501. DOI PubMed
26. Tang, J.; Wang, X.; Wang, Y.; et al. Active non-bonding oxygen mediate lattice oxygen oxidation on $NiFe_2O_4$ achieving efficient and stable water oxidation. *Chin. J. Catal.* **2025**, *72*, 164-75. DOI
27. Avcl, Ö. N.; Sementa, L.; Fortunelli, A. Mechanisms of the oxygen evolution reaction on $NiFe_2O_4$ and $CoFe_2O_4$ inverse-spinel oxides. *ACS. Catal.* **2022**, *12*, 9058-73. DOI PubMed PMC
28. Zhang, X.; Zhang, J.; Ma, Z.; et al. Ag engineered NiFe-LDH/$NiFe_2O_4$ Mott-Schottky heterojunction electrocatalyst for highly efficient oxygen evolution and urea oxidation reactions. *J. Colloid. Interface. Sci.* **2024**, *665*, 313-22. DOI PubMed
29. Peng, K.; Bhuvanendran, N.; Zhang, W.; Pasupathi, S.; Su, H. Strong interfacial coupling activates lattice oxygen of heterogeneous cerium hydroxide/nickel ferrite catalyst for robust oxygen evolution reaction performance. *Composites. Part. B. Eng.* **2026**, *309*, 113080. DOI
30. Li, X.; Wang, M.; Fu, J.; Lu, F.; Li, Z.; Wang, G. Sulfurized $NiFe_2O_4$ electrocatalyst with in situ formed Fe-NiOOH nanoparticles to realize industrial-level oxygen evolution. *Small* **2024**, *20*, e2310040. DOI PubMed
31. Yao, L.; Wu, X.; Geng, Z.; et al. Oxygen evolution reaction of amorphous/crystalline composites of $NiFe(OH)_x$/$NiFe_2O_4$. *ACS. Nano.* **2025**, *19*, 5851-9. DOI
32. Li, Y.; Zhang, Z.; Li, C.; et al. Introducing phosphorus into spinel nickel ferrite to enhance lattice oxygen participation towards water oxidation electrocatalysis. *Appl. Catal. B. Environ. Energy.* **2024**, *355*, 124116. DOI
33. Zhang, Z.; Li, Y.; Zhong, Y.; et al. sp^2/sp^3-hybridized nitrogen-mediated electrochemical CO_2 capture and utilization. *Sci. Adv.* **2025**, *11*, eadw6592. DOI

34. Tao, Y.; Jiang, W.; Wang, H.; et al. Tuning electronic structure of hedgehog-like nickel cobaltite via molybdenum-doping for enhanced electrocatalytic oxygen evolution catalysis. *J. Colloid. Interface. Sci.* **2024**, *657*, 921-30. DOI PubMed
35. Yang, B.; Bai, Z. P.; Cui, R. D.; Zeng, X. F.; Wang, J. X. A facile Mo doping strategy for high-entropy spinel oxide towards efficient oxygen evolution reaction. *AIChE. J.* **2025**, *71*, e70087. DOI
36. Li, X.; Gou, J.; Bo, L.; et al. Quenching induced Cu and F co-doping multi-dimensional Co_3O_4 with modulated electronic structures and rich oxygen vacancy as excellent oxygen evolution reaction electrocatalyst. *J. Colloid. Interface. Sci.* **2025**, *690*, 137288. DOI PubMed
37. Yue, Y.; Zhong, X.; Sun, M.; et al. Fluorine engineering induces phase transformation in $NiCo_2O_4$ for enhanced active motifs formation in oxygen evolution reaction. *Adv. Mater.* **2025**, *37*, e2418058. DOI PubMed
38. Cheng, J.; Zhang, Z.; Li, X.; et al. High-entropy spinel oxide nanoparticles with surface anionic Mo Species for seawater oxidation. *ACS. Appl. Nano. Mater.* **2025**, *8*, 14999-5007. DOI
39. Ding, S.; Duan, J.; Chen, S. Recent advances of metal suboxide catalysts for carbon-neutral energy applications. *EcoEnergy* **2024**, *2*, 45-82. DOI
40. Hong, X.; Gao, Y.; Ji, M.; et al. Highly valent cobalt-manganese spinel nanowires induced by fluorine-doping for durable acid oxygen evolution reaction. *J. Alloys. Compd.* **2024**, *1007*, 176500. DOI
41. Xiao, K.; Wang, Y.; Wu, P.; Hou, L.; Liu, Z. Q. Activating lattice oxygen in spinel $ZnCo_2O_4$ through filling oxygen vacancies with fluorine for electrocatalytic oxygen evolution. *Angew. Chem. Int. Ed.* **2023**, *62*, e202301408. DOI PubMed
42. Ping, X.; Liu, Y.; Zheng, L.; et al. Locking the lattice oxygen in RuO_2 to stabilize highly active Ru sites in acidic water oxidation. *Nat. Commun.* **2024**, *15*, 2501. DOI PubMed PMC
43. Li, Y.; Guo, H.; Zhao, J.; Zhang, Y.; Zhao, L.; Song, R. Te-doped $NiFe_2O_4$ stabilized by amorphous carbon layers derived from one-step topological transitions of NiFe LDHs with significantly enhanced oxygen evolution reaction. *Chem. Eng. J.* **2023**, *464*, 142604. DOI
44. Xiang, W.; Hernandez, S.; Hosseini, P.; et al. Unveiling surface species formed on Ni-Fe spinel oxides during the oxygen evolution reaction at the atomic scale. *Adv. Sci.* **2025**, *12*, e2501967. DOI PubMed PMC
45. Li, Y.; Zhang, Z.; Li, C.; et al. Cation-vacancy-induced reinforced electrochemical surface reconstruction on spinel nickel ferrite for boosting water oxidation. *Adv. Funct. Mater.* **2024**, *35*, 2417983. DOI
46. He, Y.; Zhang, L.; Xiong, H.; Kang, X. Evolution of lattice defects in nickel ferrite spinel: Oxygen vacancy and cation substitution. *J. Alloys. Compd.* **2022**, *917*, 165494. DOI
47. Zhang, H.; Zhao, Y.; Cheng, Z.; Jiang, J.; Fu, J.; Xu, Q. 2D $NiFe_2O_4$/$Ni(OH)_2$ heterostructure-based self-supporting electrode with synergistic surface/interfacial engineering for efficient water electrooxidation. *Small* **2024**, *20*, e2405225. DOI PubMed
48. Luong, T. N.; Doan, T. L. L.; Bacirhonde, P. M.; Park, C. H. A study on synthesis of an advanced electrocatalyst based on high-conductive carbon nanofibers shelled $NiFe_2O_4$ nanorods for oxygen evolution reaction. *Int. J. Hydrogen. Energy.* **2025**, *99*, 1108-18. DOI
49. Triolo, C.; Moulaee, K.; Bellato, F.; et al. Interplay between alkaline water oxidation temperature, composition and performance of electrospun high-entropy non-equimolar (Cr,Mn,Fe,Co,Ni) oxide electrocatalysts. *J. Power. Sources.* **2025**, *654*, 237887. DOI
50. Tan, J.; Ma, M.; Cheng, S.; et al. Isolated Mo-doped nickel-iron spinel catalyst with oxygen vacancy and high-density interfaces for oxygen evolution reaction. *Int. J. Hydrogen. Energy.* **2025**, *137*, 73-82. DOI
51. Wu, W.; Liu, B.; Xu, X.; Jing, P.; Li, L.; Zhang, J. Synergistically regulating the electronic structure and stabilizing the lattice oxygen of spinel cobalt oxide by Mo and Pr dual doping to enhance acidic oxygen evolution performance. *Inorg. Chem.* **2025**, *64*, 12174-88. DOI PubMed
52. Wang, Y.; Feng, H.; Chai, D. F.; et al. Rapid and in-depth reconstruction of fluorine-doped bimetallic oxide in electrocatalytic oxygen evolution processes. *J. Colloid. Interface. Sci.* **2025**, *684*, 84-94. DOI PubMed
53. Zhao, H.; Zhu, L.; Yin, J.; et al. Stabilizing lattice oxygen through Mn doping in $NiCo_2O_{4-\delta}$ spinel electrocatalysts for efficient and durable acid oxygen evolution. *Angew. Chem. Int. Ed.* **2024**, *63*, e202402171. DOI PubMed
54. Peng, Y.; Huang, C.; Huang, J.; et al. Filling octahedral interstices by building geometrical defects to construct active sites for boosting the oxygen evolution reaction on $NiFe_2O_4$. *Adv. Funct. Mater.* **2022**, *32*, 2201011. DOI
55. Yan, Y.; Lin, J.; Huang, K.; et al. Tensile strain-mediated spinel ferrites enable superior oxygen evolution activity. *J. Am. Chem. Soc.* **2023**, *145*, 24218-29. DOI PubMed

Disclaimer/Publisher's Note: All statements, opinions, and data contained in this publication are solely those of the individual author(s) and contributor(s) and do not necessarily reflect those of OAE and/or the editor(s). OAE and/or the editor(s) disclaim any responsibility for harm to persons or property resulting from the use of any ideas, methods, instructions, or products mentioned in the content.

© The Author(s) 2026. Open Access This article is licensed under a Creative Commons Attribution 4.0 International License (https://creativecommons.org/licenses/by/4.0/), which permits unrestricted use, sharing, adaptation, distribution and reproduction in any medium or format, for any purpose, even commercially, as long as you give appropriate credit to the original author(s) and the source, provide a link to the Creative Commons license, and indicate if changes were made.